

A bioprinted human-glioblastoma-on-a-chip for the identification of patient-specific responses to chemoradiotherapy

Hee-Gyeong Yi^{1,11}, Young Hun Jeong^{2,11}, Yona Kim³, Yeong-Jin Choi^{4,5}, Hyo Eun Moon³, Sung Hye Park⁶, Kyung Shin Kang⁷, Mihyeon Bae¹, Jinah Jang^{8,9}, Hyewon Youn¹⁰, Sun Ha Paek^{3*} and Dong-Woo Cho^{1*}

Patient-specific ex vivo models of human tumours that recapitulate the pathological characteristics and complex ecology of native tumours could help determine the most appropriate cancer treatment for individual patients. Here, we show that bioprinted reconstituted glioblastoma tumours consisting of patient-derived tumour cells, vascular endothelial cells and decellularized extracellular matrix from brain tissue in a compartmentalized cancer-stroma concentric-ring structure that sustains a radial oxygen gradient, recapitulate the structural, biochemical and biophysical properties of the native tumours. We also show that the glioblastoma-on-a-chip reproduces clinically observed patient-specific resistances to treatment with concurrent chemoradiation and temozolomide, and that the model can be used to determine drug combinations associated with superior tumour killing. The patient-specific tumour-on-a-chip model might be useful for the identification of effective treatments for glioblastoma patients resistant to the standard first-line treatment.

Patient-specific cancer models for precision cancer medicine are expected to help determine the most appropriate treatment for an individual^{1–4}. Patient-derived tumour xenograft animal models have been shown to reproduce the characteristics of the parental tumours well^{5,6}, but their clinical use for point-of-care testing has been hindered by the long time required for their establishment, low success rates, high costs and ethical issues^{3,4,6}. Establishing an ex vivo cancer model can overcome some of these disadvantages^{3,4,7,8}. Such a model needs to reflect the original identity of the parental cancer, with its multifactorial complexity, to ensure that the therapeutic responses of the patient are correctly identified^{9–11}. However, the recapitulation of the interactions between the cancer cells and the associated environmental factors—which influences the typical characteristics of cancer, such as uncontrollable cell proliferation, excessive angiogenesis and treatment resistance—is a challenge^{12–16}. Therefore, the emulation of the heterogeneous ecology of a cancer in an ex vivo model is important, enabling potential drugs to be more reliably tested^{12,16}.

Current ex vivo cancer models still have limitations with regards to creating a physiologically relevant system that includes the cellular and molecular diversity as well as the biochemical and biophysical cues of the cancer. It has been shown with hydrogel-based cancer models that the three-dimensional (3D) microenvironment and its biochemical properties are crucial for reproducing the interactions between cells and the extracellular matrix (ECM)^{17–19}. However, the conventional hydrogels poorly mimic the complex molecular composition of the native ECM and its associated interactions with

cells. Microfluidics-based cancer models (cancers-on-chips) have allowed for precise biophysical manipulation by mimicking how cancer cells are subjected to an oxygen gradient²⁰ and to regional events occurring between the tumour cells and associated cells (for example, tumour angiogenesis)^{21,22}. However, with current models it is not straightforward to construct a complex cancer system that allows for extensive interactions with the various compartmentalized tissues, ECM molecules and physiological factors.

Here, we present an approach for producing an ex vivo cancer model with a highly biomimetic ecosystem that provides the important cues for recapitulating the pathological features of glioblastoma (GBM), thus allowing for patient-specific drug susceptibility to be identified (Fig. 1). GBM is the most common brain cancer, which accounts for around 50% of all malignant primary brain tumours²³ and is highly lethal. Our strategy involves simultaneously mimicking the biochemical and biophysical properties of the native GBM using a 3D bioprinting process. In this way, we created a cancer analogue on a chip that combines a compartmentalized cancer-stroma structure, an oxygen-gradient-generating system and brain decellularized ECM (BdECM). We found that this high level of heterogeneity significantly contributed to the emergence of the various pathological features of GBM. The GBMs-on-chips printed with patient-derived cancer cells produced differential responses that matched the clinical outcomes after concurrent chemoradiation (CCRT) using temozolomide (TMZ). Furthermore, the GBMs-on-chips exhibited patient-specific sensitivity against potential drug combinations. The results of this approach suggest that an ex vivo

¹Department of Mechanical Engineering, POSTECH, Pohang, Korea. ²School of Mechanical Engineering, Kyungpook National University, Daegu, Korea.

³Department of Neurosurgery, Cancer Research Institute and Ischemic/Hypoxic Disease Institute, Seoul National University College of Medicine, Seoul, Korea. ⁴Division of Integrative Biosciences and Biotechnology, POSTECH, Pohang, Korea. ⁵Powder & Ceramics Division, Korea Institute of Materials Science, Changwon, Korea. ⁶Department of Pathology, Seoul National University College of Medicine, Seoul, Korea. ⁷School of Physical Sciences and Engineering, Anderson University, Anderson, IN, USA. ⁸Department of Creative IT Engineering, POSTECH, Pohang, Korea. ⁹School of Interdisciplinary Bioscience and Bioengineering, POSTECH, Pohang, Korea. ¹⁰Department of Nuclear Medicine and Cancer Research Institute, Seoul National University College of Medicine, Seoul, Korea. ¹¹These authors contributed equally: Hee-Gyeong Yi, Young Hun Jeong. *e-mail: paeksh@snu.ac.kr; dwcho@postech.ac.kr

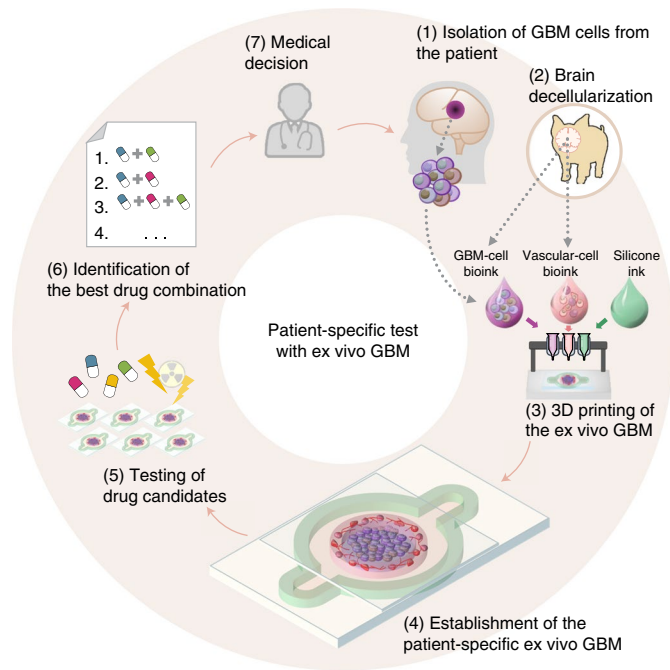


Fig. 1 | Schematic illustration of the bioprinting and use of the patient-specific GBM-on-a-chip for the identification of an optimal drug combination for the patient. Step 1, GBM cells are isolated from a specimen obtained through removal surgery. Step 2, off-the-shelf porcine BdECM bioink is obtained. Step 3, patient-derived cancer cells are printed with the BdECM bioink to produce a patient-specific GBM-on-a-chip. To mimic the heterogeneous GBM ecology, several other inks are used in the printing process, including a vascular cell-laden BdECM bioink and a silicone ink. Step 4, the chip is cultured for 1–2 weeks to recapitulate the pathological features. Step 5, various candidate drug combinations are tested using the chip. Step 6, the drug combinations are prioritized according to their efficiencies and the best combination is identified. Step 7, the physician uses the test results to design a treatment plan for the patient.

system is an option for modelling personalized cancer treatments and for guiding clinical decisions that may overcome refractory cancers.

Brain-derived-ECM bioink

The ECM is composed of diverse macromolecules that determine the tissue-specific distinctive biochemical and biomechanical properties, and is an essential factor in cancer progression^{9,24}. However, it would be virtually impossible to find a combination of purified natural or man-made materials that optimally reproduce the intrinsic complexity of native ECM; decellularized ECM (dECM) is, therefore, considered ideal for providing a microenvironment comparable to that of the parental tissue. It has recently been demonstrated that cancer cells seeded onto dECM materials exhibit upregulated expression of various genes related to invasion and to interactions between the cells and ECM molecules^{25,26}. However, when seeding cells onto dECMs, it is difficult to control the distribution and location of different cell types to reconstitute the heterogeneous tissue.

To print the GBM-on-a-chip with congenital brain ECM composition, we developed a bioink solution composed of BdECM. The bioink serves as a protective encapsulating carrier for cells during their passage through a printing nozzle and then becomes a cell-supporting matrix through solidification after deposition. The BdECM bioink was generated through modifications of the preparation procedures for other dECM bioinks that we developed

previously^{27,28}. Porcine brain was decellularized with the serial treatment of chemical and enzymatic agents. By altering the decellularization parameters, we established the appropriate conditions for the effective removal of the double-stranded DNA content (achieving approximately 99% reduction) while reducing the damage to the ECM components, such as glycosaminoglycan (approximately 142% retention) and hyaluronic acid (approximately 69% retention; Fig. 2a–f and Supplementary Fig. 1a). The BdECM was then solubilized as a viscous solution. When warmed to a physiological temperature, it exhibited thermosensitive sol–gel transition kinetics (Fig. 2g,h and Supplementary Fig. 1b).

We assessed the potential of the BdECM bioink in promoting the malignancy of the cultured GBM cells compared with collagen gel. We performed a hydrogel-embedding culture to mimic cells growing in an encapsulated form after the 3D-bioprinting process. Commercially obtained human GBM cells (U-87, a GBM-like cell line from the ATCC) were embedded in the BdECM and collagen gels. Both hydrogels demonstrated >90% cell viability (Supplementary Fig. 1c), but proliferation was higher in the BdECM gel than the collagen gel after 10 days (Fig. 2i). The GBM cells in the BdECM gel also demonstrated higher expression levels of genes that encode pro-angiogenic factors (*VEGFA* and *IL8*) and the ECM-remodelling proteins (*PTK2*, *FN*, *MMP1*, *MMP2* and *MMP9*) at three days (Fig. 2j). Correspondingly, in a cancer-spheroid-invasion study, GBM-28 cells (isolated from patient f, see Supplementary Table 3) showed increased invasion and a more spindle-like morphology in the BdECM gel, than the collagen gel (Fig. 2l). These morphological changes corresponded to the collective cell migration and the elongated form of the invasive cells observed in the GBM²⁹. The BdECM gel also exhibited a superior capacity with regard to the angiogenesis of human umbilical vein endothelial cells (HUVECs). Compared with those embedded in collagen, HUVECs in the BdECM gel showed increased expression of the genes related to cell junction molecules (*PECAM1*, *CDH5* and *TJPI*) and ECM-remodelling protein (*MMP9*; Fig. 2k). CD31⁺-endothelial cells formed tubule networks more actively in the BdECM gel than in the collagen gel over two weeks (Fig. 2m).

Key environmental properties in the GBM-on-a-chip

GBM grows in a highly dense spherical shape, which forms anatomically distinct regions (core, intermediate and peripheral) along an oxygen gradient (Fig. 3a,e). The cancer cells in the core region experience severe hypoxia and form a necrotizing zone with pseudopalisading cells. In the intermediate region, anaplastic cells proliferate excessively and secrete many cytokines for survival. As a result, invasion and hyperplasia of microvessels occur in the peripheral region of the cancer.

To represent the heterogeneous ecology of a GBM, the principles underlying the model were to surround the cancerous tissue with microvessels and to induce central hypoxia. The GBM-on-a-chip was therefore composed of innermost cancer cells, surrounding vascular endothelial cells and an outermost chamber filled with culture medium. Using an in-house 3D-printing system³⁰, the chip was fabricated as follows: (1) the chamber wall was printed with gas-permeable silicone ink on a non-permeable glass substrate; (2) to construct the GBM-mimetic structure, BdECM bioink laden with HUVECs was first printed in a ring shape; (3) BdECM bioink laden with GBM cells was then printed to fill the inside of the BdECM–HUVEC ring structure and (4) the whole printed construct was solidified in a humidified cell culture incubator and the top of the chamber was then covered with a glass cover slip (Fig. 3b,c and Supplementary Video 1). The culture medium was fed through an inlet hole in the silicone chamber (containing a second hole to balance the pressure).

Because oxygen was available to the cells only via the gas-permeable chamber wall, oxygen consumption by the cells resulted

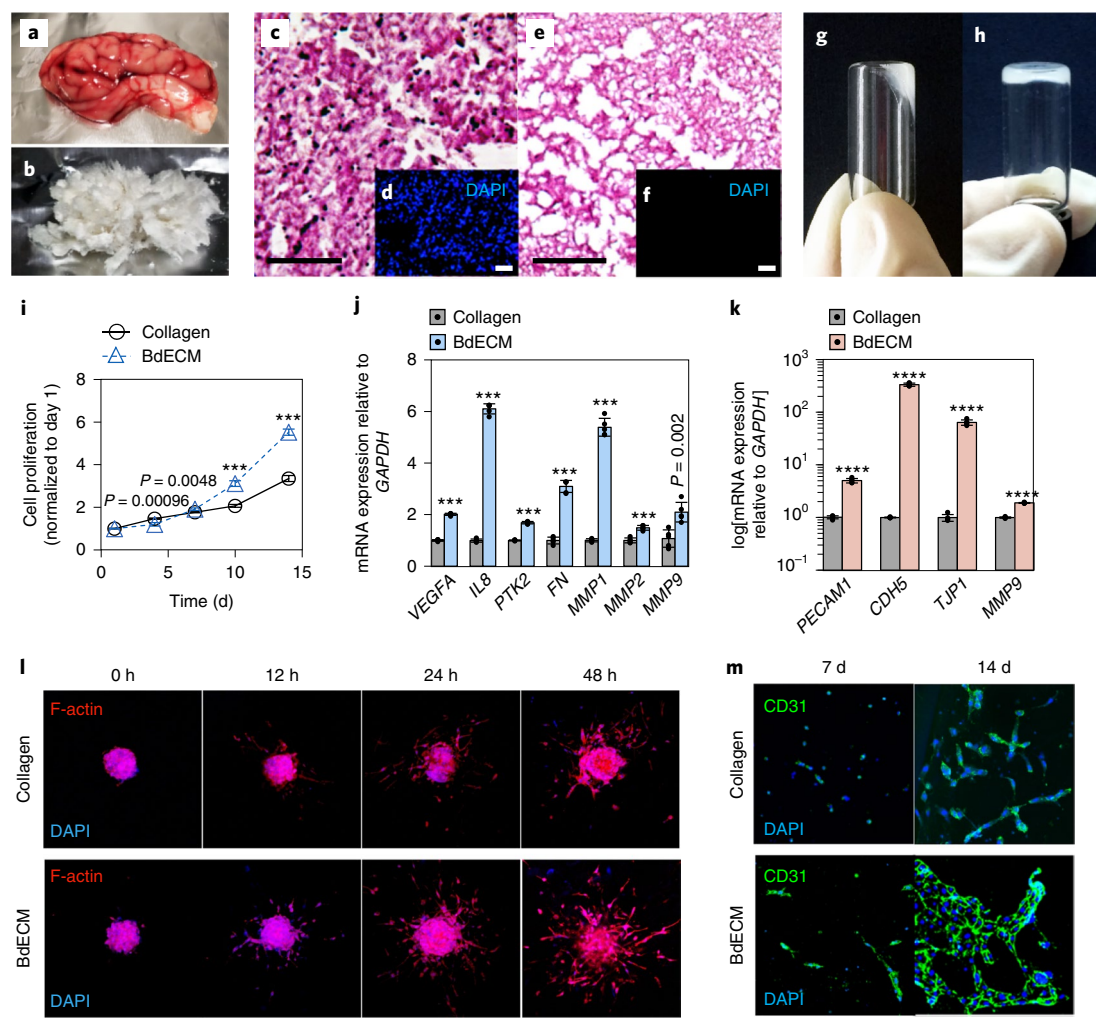


Fig. 2 | Preparation and evaluation of the BdECM bioink. a, b, Photographs of native porcine brain tissue (**a**) and decellularized brain (**b**). **c–f**, Representative images of haematoxylin and eosin (**c, e**), and DAPI (**d, f**) staining of native brain tissue (**c, d**) and decellularized brain tissue (**e, f**). $n = 5$ for both the native brain tissue and BdECM. Scale bars, 200 μm . **g, h**, Photographs before (**g**) and after (**h**) gelation of the BdECM pre-gel solution. **i**, Proliferation (normalized to the count at day 1) of the GBM cells embedded in either collagen or BdECM gel ($n = 4$). **j, k**, Changes in the levels of messenger RNA expression of various genes in GBM cells (**j**) and HUVECs (**k**) embedded either in collagen or BdECM gel ($n = 5$). The error bars represent the s.d. $***P < 0.001$, $****P < 0.0001$; paired two-tailed Student's *t*-tests. **l**, Representative time-lapse fluorescent microscope images of the invasive cells from GBM-28 spheroids embedded in either collagen or BdECM gel for 48 h. $n = 3$ for each experimental group. Scale bar, 200 μm . The total area of fluorescence is described in Supplementary Fig. 1d. **m**, Representative immunostaining images of endothelial cells using CD31 for the adhesion molecules and DAPI for the cell nuclei. Scale bar, 100 μm .

in a radial oxygen gradient. To simulate the oxygen concentration distribution in this design, we performed computational finite element analysis, which demonstrated the formation of central hypoxia in the chamber composed of selectively gas-permeable parts (Fig. 3d and Supplementary Fig. 2). However, it is difficult to calculate the exact oxygen concentration, which varies according to the change of cellular activity, in a simulation. Thus, we observed the regional difference in hypoxia experimentally by immunofluorescent staining with pimonidazole, a hypoxia marker, and Ki67 protein, a proliferation marker. Although we changed the culture medium every day, the number of hypoxic cells increased from the peripheral to the core regions over three days (Fig. 3e, f). Proliferating cells showed the opposite tendency (that is, the number of Ki67⁺ cells decreased). In addition, invasive cells were observed in the peripheral region due to the migration of cancer cells towards the outer region with a relatively high oxygen level (Fig. 3g). Real-time imaging also showed the invasive cells heading

into the surrounding region on which the bioink with no cells was printed (Supplementary Video 2).

Recapitulation of the pathological features of GBM

The GBM-on-a-chip simultaneously captured the three key properties of the original cancer environment: a biochemical cue (the brain-ECM-like microenvironment) and two biophysical cues (the compartmentalized structure of the cancerous mass surrounded by the vascularized stroma and the oxygen gradient). We evaluated the effect of these properties on the recapitulation of the pathophysiology of GBM by comparing different combinations of environmental cues (Fig. 4a). For this comparison, we denoted the compartmentalized structure by separately printing each cell type as SP⁺ (SP⁻ indicates non-compartmentalized cells). We also denoted the presence and absence of an oxygen gradient as GR⁺ and GR⁻, respectively. For the SP⁻GR⁺ condition, we mixed GBM cells and HUVECs into a single BdECM bioink, printed the cellular construct with a random

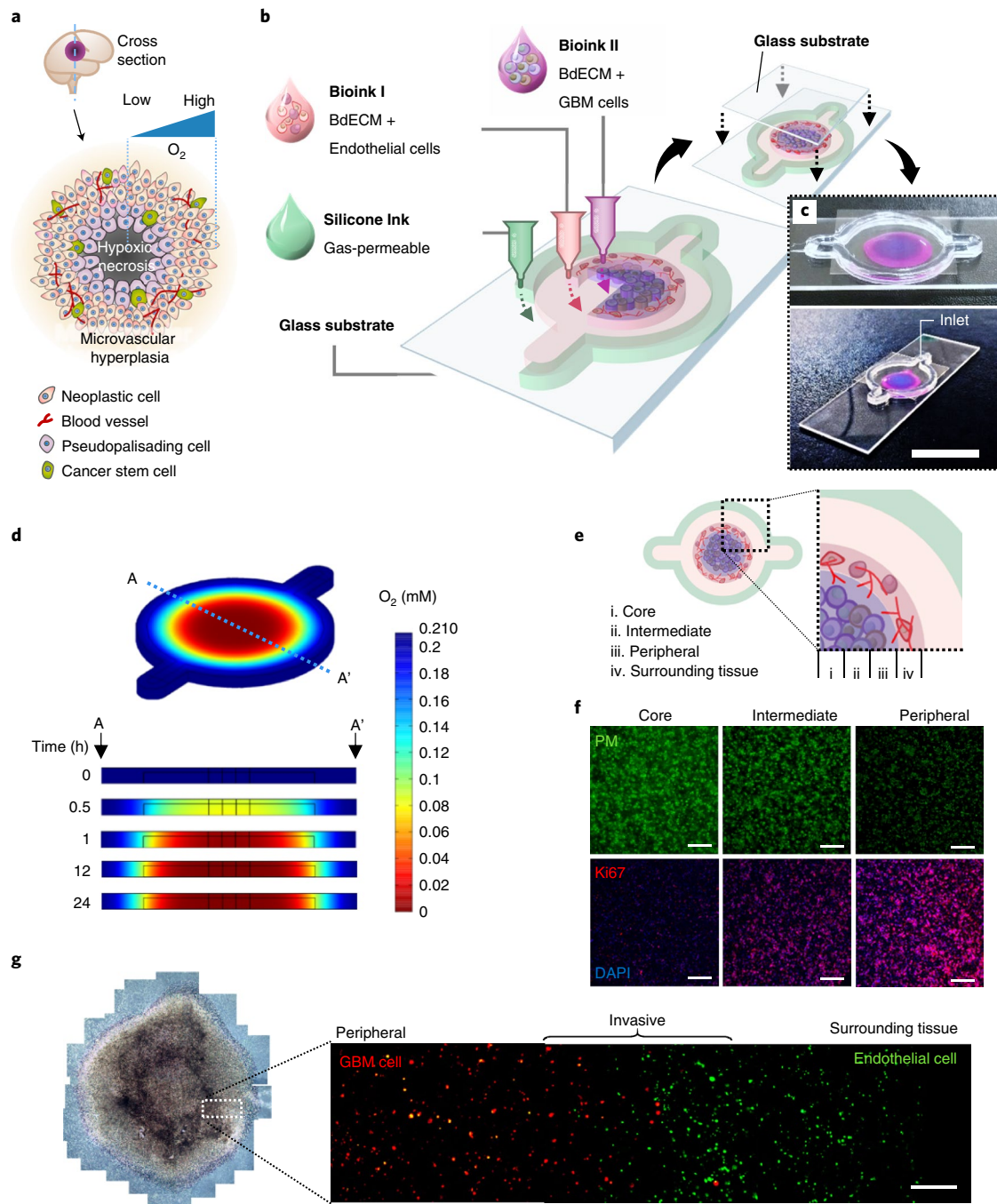


Fig. 3 | Working principles of the GBM-on-a-chip and confirmation of reconstituted GBM ecology. **a**, Schematic illustration of a cross-sectional view of a native GBM. **b**, Schematic illustration of the process for printing the GBM-on-a-chip with various bioinks and other materials to construct a compartmentalized structure. **c**, Photographs of a mock GBM-on-a-chip including the BdECM bioink laden with HUVECs (magenta) or GBM cells (blue) shown from above (top) and from the corner (bottom). Scale bar, 2 cm. **d**, Time-lapse jet colourmap images of oxygen concentrations along the cross section A-A' calculated by computer simulation. **e**, Schematic drawing of the (i) core, (ii) intermediate and (iii) peripheral regions within the printed GBM and (iv) the surrounding tissue region in the part printed with HUVECs. **f**, Immunostaining images of the different regions using pimonidazole (PM) for the hypoxic cells, Ki67 for the proliferating cells and DAPI for the cell nuclei. Scale bar, 200 μm . **g**, Representative images of the GBM-on-a-chip observed by phase-contrast optical (left) and fluorescence microscopy (right) with the GBM cells labelled with Dil and HUVECs labelled with DiO ($n=3$). Scale bar, 500 μm .

distribution and covered the chamber with the glass substrate to block oxygen penetration, thus generating an oxygen gradient. For the SP^+GR^- condition, we printed the GBM and HUVEC bioinks separately as before but covered the chamber with a thin silicone film, which allows gas permeation from above and resulted in a consistent oxygen distribution across the chamber. For the

SP^+GR^+ condition—that is, the model itself—the compartmentalized structure was printed and covered with the glass substrate.

The different environmental combinations influenced the formation of the pseudopalisades. By day 7, compared with the SP^-GR^+ condition, the SP^+GR^+ condition showed a higher expression of the genes related to cancer progression (Supplementary

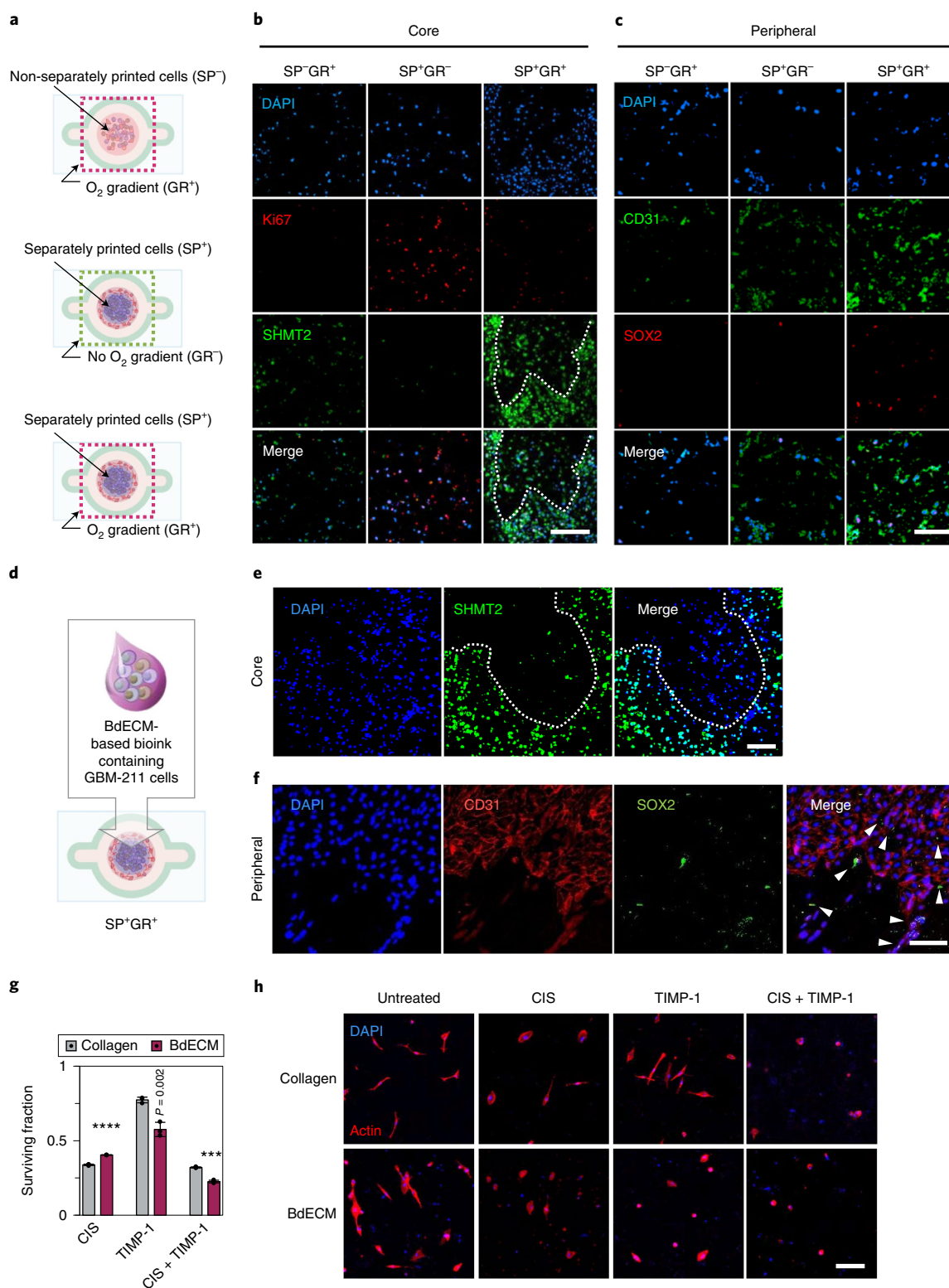


Fig. 4 | The synergistic effect of biochemical and biophysical heterogeneities on the pathological progression of GBM-on-a-chip. a,d, Schematic illustrations of the three tested conditions (**a**; SP⁻GR⁺, SP⁺GR⁻ and SP⁺GR⁺) and the SP⁺GR⁺ condition printed with GBM-211 cells (**d**). **b,e**, Representative immunostaining images using SHMT2 for the pseudopalisading cells, Ki67 for proliferating cells (only in **b**) and DAPI for the cell nuclei ($n=4$ for each experimental group). The images were observed in the core regions. The white dotted line indicates pseudopalisade formation. Scale bars, 200 μm . **c,f**, Representative immunostaining images using CD31 for HUVECs, SOX2 for resistant cancer cells and DAPI for the cell nuclei ($n=3$ or 4 for each experimental group). The images were observed in the peripheral regions. Scale bars, 200 μm (**c**) and 100 μm (**f**). The white arrowheads in **f** indicate SOX2⁺-resistant cancer cells located near CD31⁺ HUVECs. **g,h**, After treating the patient-derived GBM-211-cells-on-chips, that were printed with collagen- or BdECM-based bioink, with 950 μM CIS, 1 μgml^{-1} TIMP-1 or a combination of the two, we obtained surviving fractions (**g**; $n=4$ for each treatment) and representative actin staining images (**h**; $n=3$ for each treatment). The error bars represent the s.d. **** $P < 0.001$, **** $P < 0.0001$; paired two-tailed Student's t -tests. Scale bar, 200 μm .

Fig. 3a). Interestingly, the SHMT2⁺ cells³¹ formed a pseudopalisade surrounding the necrotic foci only under SP⁺GR⁺ conditions (Fig. 4b,e), although a TUNEL assay revealed the formation of a necrotic core with both the SP⁻GR⁺ and SP⁺GR⁺ conditions (Supplementary Fig. 3b).

The heterogeneous environment mimicking the microvessels surrounding GBM also affected the emergence of SOX2⁺-resistant cells. By day 7, the SP⁺GR⁺ condition induced the overexpression of the SOX2 and *NES* genes, indicating the promoted resistance of cancer cells (Supplementary Fig. 3a). Although CD31⁺-endothelial cells settled in the peripheral regions in both the SP⁺GR⁻ and SP⁺GR⁺ conditions, SOX2⁺-resistant cancer cells were observed only under the SP⁺GR⁺ condition. Moreover, the fragmented microvessels shown in the GBM-on-a-chip indicated the dysfunctional leaky vessel formation, as seen in the actual cancer³².

Overall, the SP⁺GR⁺ condition was superior to the other conditions in recapitulating the important pathological features of the cancer, including the hypoxia-induced necrotic core, pseudopalisading, spatial heterogeneity of cell types and the perivascular niche. Similar tendencies were also observed in the comparison of the three combinations (SP⁻GR⁺, SP⁺GR⁻ and SP⁺GR⁺) when we evaluated the pathological morphologies by substituting the BdECM bioink with collagen bioink (Supplementary Fig. 4a-d). However, the BdECM bioink was considerably more effective than the collagen bioink with regard to the overexpression of the GBM-related genes (Supplementary Fig. 4e).

After optimizing the various environmental conditions of the chip, we established a patient-specific GBM-on-a-chip by printing GBM-211 cells isolated from an aggressively invasive GBM into the environment incorporating SP⁺GR⁺ conditions and BdECM bioink (Fig. 4d). The GBM-211-on-a-chip also formed clear pseudopalisade and SOX2⁺-resistance cancer cells (Fig. 4e,f). In addition, the GBM-211 cells on chips showed different drug sensitivities depending on the bioink types. GBM-211 cells printed with BdECM bioink were less responsive to cisplatin (CIS)³³ treatment compared with cells printed with collagen bioink (Fig. 4g). However, GBM-211 cells in the BdECM bioink were more sensitive to tissue inhibitors of metalloproteinases-1 (TIMP-1)³⁴, an anti-invasion agent, compared with the cells in collagen bioink. The more apparent morphological change was also exhibited in BdECM-bioink conditions following TIMP-1 treatment (Fig. 4h). Thus, we assume that the enriched biochemical cues of BdECM bioink strongly influenced the sensitivity of cancer cells against the anti-invasion agent, which inhibits interactions between the cells and the ECM. These data again support the idea that the synergistic effects of the BdECM, oxygen gradient and compartmentalized tissue structure are crucial for the recapitulation of the original GBM pathophysiology.

Replication of patient-specific treatment responses

Next, we examined the ability of the GBM-on-a-chip to reproduce the differences in treatment resistance observed in GBM patients. The GBMs-on-chips were printed with primary GBM cells obtained from patients showing very different manifestations in the clinic. The prognosis of the GBM patients varied following CCRT with TMZ, which is the current standard of care for GBM (Fig. 5a and Supplementary Table 3). One group of patients (a, b and c; Group X) exhibited low-to-moderate treatment resistance and survived for >2 yrs. Another group of patients (d and e; Group Y) showed high resistance to treatment and survived for <1 yr. The final group of patients (f and g; Group Z) experienced extremely aggressive tumour progression following CCRT. From the three groups of patients, GBM-15, -26, -278, -211, -28 and -51 cells were obtained during brain-tumour-removal surgery before receiving CCRT. Whereas, GBM-37 and -103 cells were obtained from the tumours following CCRT.

Given these clinical observations, we evaluated the treatment resistances shown by the patient-derived GBM cells. First, we compared the responses to CCRT with TMZ of the GBM-28 and -37 cells when the cells were cultured in the developed chip as well as conventional systems, such as monolayer and spheroid-culture systems (Supplementary Fig. 5a,b). Although the cells in all culture systems showed a dose-dependent reduction in the percentage of survival, the difference in responsiveness between the GBM-28 and -37 cells was not seen in those conventional systems. Moreover, when we established the GBMs-on-chips under GR⁻ and GR⁺ conditions and compared the resistance to treatment shown by GBM-28 and -37 cells on chips, the GR⁺ condition exhibited greater differences in the resulting levels of resistance (Supplementary Fig. 5c). Furthermore, the half-maximal inhibitory concentrations (IC₅₀) of TMZ (950 μM) and radiation (15 Gy) determined from the GBM-28 cells on the chip were notably higher than those of the monolayer (IC₅₀ < 500 μM with 3 Gy irradiation) and the spheroid-culture systems (IC₅₀ < 200 μM with 5 Gy irradiation; Supplementary Figs. 5a,b and 6a,b). We speculated that the reconstitution of the complex environment of the GBM-on-a-chip was responsible for the increase of treatment resistance of the patient-derived GBM cells and thereby led to the differentiation of the responsiveness between the GBM-28 and -37 cells against the treatment, as seen in the clinics. Together, the GBM-on-a-chip with the highly biomimetic condition was more efficient in predicting the efficacies of the tested treatments compared with the conventional culture systems^{35–37}.

We then compared the survival percentage of the GBMs-on-chips following the single-fraction of CCRT with TMZ. The survival percentages observed for the GBM-15, -26 and -278 cells on chips (Group X) was lower than that of the other groups, whereas the GBM-28, -37, -51 and -103 cells on chips (Group Z) showed considerably higher levels of survival percentages (Fig. 5b). Interestingly, the order of the percentage of survival obtained from the GBMs-on-chips following a single-fraction treatment was X < Y < Z, which reflects the differences in treatment resistance observed in the clinical setting. Similar trends were maintained even when the TMZ dose was lowered to 400 μM or the radiation dose increased to 30 Gy (Supplementary Fig. 6c). More interestingly, the patient-derived GBMs reproduced the differing responses of the tumours on the chips following multiple CCRTs with TMZ (treatment every three days, five times in total; Fig. 5c). The GBM-26 cells derived from the patient who showed the most favourable treatment outcome exhibited a steady decrease in metabolic activity on the chip even after the conclusion of treatment. In contrast, the GBM-28 and -51 cells derived from the patients who experienced increased tumour progression following treatment reproduced increase in metabolic activity on the chips following treatment. Together, the decrease in the survival percentage of GBMs-on-a-chip was positively correlated with the overall survival of the patient donors (Supplementary Fig. 6d,e). These results suggest that the established method to create a GBM-on-a-chip is feasible and accurately reproduces the treatment resistance of the patient.

Evaluation of combinations of drug candidates

Finally, to find a patient-specific drug combination, we investigated the capability of the 3D-printed GBM-on-a-chip. Due to the unexpected deterioration of Patient c following CCRT with TMZ, we sought a tailored treatment for GBM-28 to prevent such aggressive transition to GBM-37. To resolve this, we identified the genetic characteristics of the GBM-28 and -37 cells and then nominated several drug candidates. Gene set enrichment analysis (GSEA) suggested that the cell-cycle-checkpoint-related gene set derived from the Reactome database is highly enriched in GBM-28 cells compared with GBM-37, suggesting an abnormality in the DNA damage response pathways of GBM-37 compared with GBM-28 (Fig. 6a,b). Dysfunctional cell-cycle checkpoints are known to play a critical

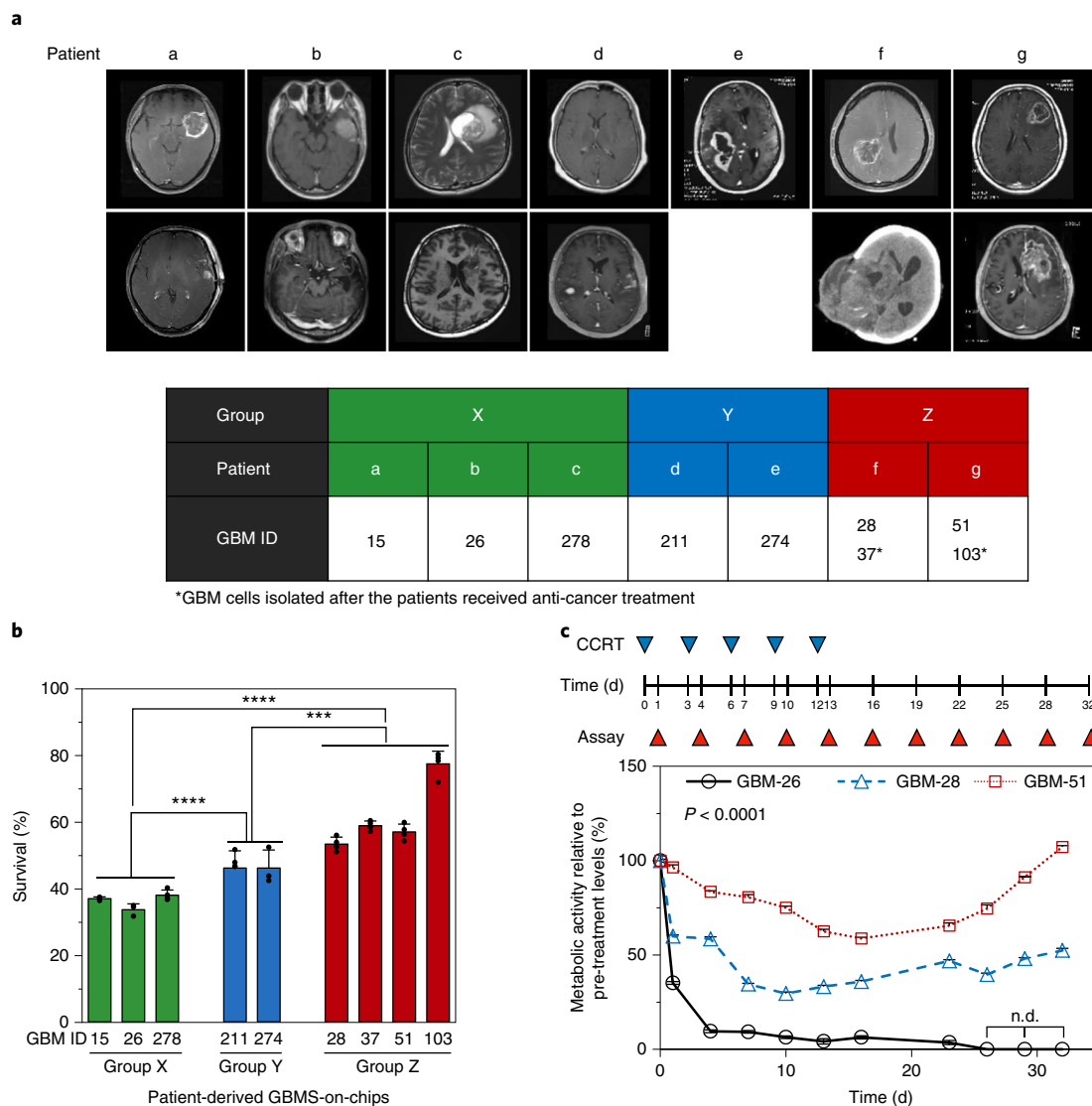


Fig. 5 | Reproduction of differences in treatment resistance in patient-specific GBMs-on-chips. a, Representative brain magnetic resonance images of the GBM patients with distinct clinical observations. The table describes the relevant notations for the patients and the patient-derived GBM cells. The preoperative images (top) show the mass lesions of each patient. The final follow-up images (bottom) show decreased mass lesions (Patients a and c), a mass lesion that became undetectable (Patient b), multiple enhanced mass lesions (Patient d), a huge bulging mass lesion protruding from the right temporoparietal craniotomy site (Patient f) and a largely enhanced mass lesion (Patient g). A final follow-up image was not obtained for Patient e. **b**, Percentage survival of the GBMs-on-chips following a single-fraction of CCRT (15 Gy) with 950 μ M TMZ ($n=3-5$ for each experimental group). The error bars represent the s.d. *** $P < 0.001$, **** $P < 0.0001$; one-way analysis of variance (ANOVA) and Bonferroni post-hoc tests. **c**, Long-term follow-up of metabolic activity changes in the GBM-26, -28 and -51 cells on chips following treatment with multiple-fractions of CCRT (3 Gy) with 250 μ M TMZ ($n=5$ for each experimental group). The diagram at the top shows the time points of the CCRT and the measurement of metabolic activity of the GBMs-on-chips. The error bars represent the s.d.; n.d., not detected. The differences between the experimental groups were analysed using one-way ANOVAs.

role in promoting tumour growth³⁸. Thus, it can be speculated that one possible crucial event resulting in the recurrence of the tumour in a more aggressive form after CCRT was defective in the cell-cycle checkpoints of the GBM-37 cells. In light of this finding, we assumed that blocking the DNA damage response would be more effective for the GBM-28 cells following the genotoxic treatments.

To find a stronger genotoxic agent, we first compared the toxicity of CCRT treatment with either TMZ or cisplatin (CIS; Fig. 6c). The survival percentage of the GBM-28 cells was notably lower after CIS treatment compared with TMZ treatment. In contrast, GBM-37 cells showed a slight decrease in the survival percentage following CIS treatment. We then combined KU60019 (KU)³⁹ with CIS to inhibit ataxia-telangiectasia mutated kinase, which

activates key proteins that initiate DNA-damage-response pathways. Surprisingly, CIS + KU suppressed the survival percentage of GBM-28-on-a-chip, whereas GBM-37-on-a-chip was less responsive to this combination.

Furthermore, we investigated whether the inhibition of DNA repair mechanisms following genotoxic treatment is also effective on the GBM-28-on-a-chip. We tested two kinds of inhibitors of the DNA repair mechanism with CCRT using TMZ treatment: O⁶-benzylguanine (O⁶BG), a pseudosubstrate of O⁶-methylguanine-DNA methyltransferase⁴⁰ and methoxyamine (MX), a base excision repair pathway inhibitor⁴¹. Both O⁶BG and MX decreased the survival percentages of GBM-28 and -37 on chips, but the GBM-28-on-a-chip showed higher susceptibility to these drugs compared with the GBM-37-on-a-chip

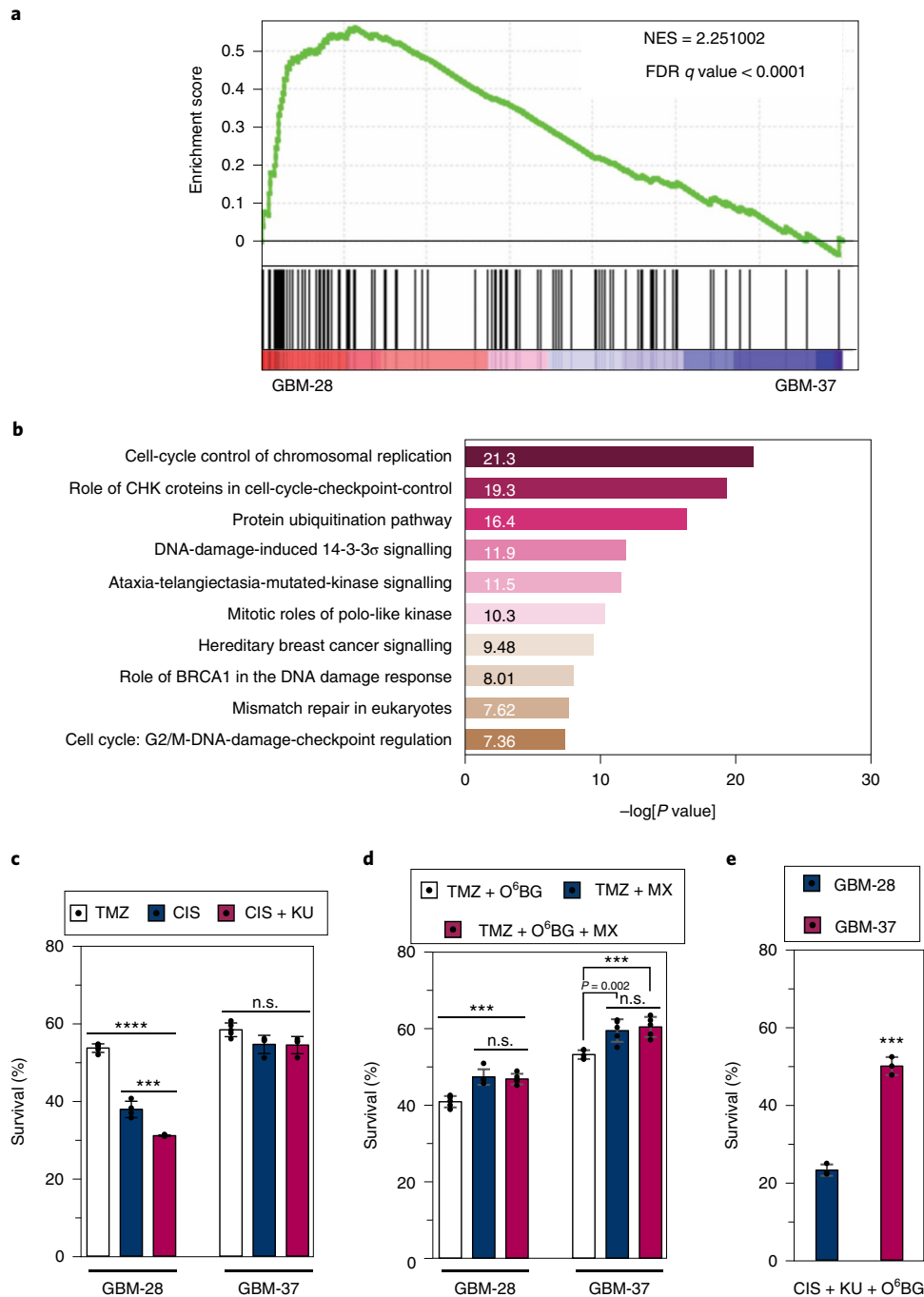


Fig. 6 | Evaluation of the susceptibility of an individual patient to CCRT with different drug combinations. **a**, The enrichment of a gene set from the Reactome database associated with cell-cycle checkpoints in GBM-28 compared with GBM-37 cells. NES, normalized enrichment score; FDR, false discovery rate. **b**, The top ten canonical pathways derived from genes in the leading edge of GSEA, analysed using IPA. **c–e**, Percentage survival of GBM-28 and -37 cells on chips after receiving CCRT with TMZ, CIS or CIS + 250 μ M KU (**c**); CCRT with TMZ + O⁶BG, TMZ + MX or TMZ + O⁶BG + MX (**d**) and CCRT with CIS + KU + O⁶BG (**e**). The concentrations of the drugs used for the experiment were 950 μ M of TMZ, 950 μ M of CIS, 250 μ M of KU, 210 μ M O⁶BG, and 150 μ M of MX. The irradiation dose was 15 Gy. The error bars represent the s.d. *** P < 0.001, **** P < 0.0001 and n.s., not significant; one-way ANOVA and Bonferroni post-hoc tests.

(Fig. 6c,d). Among the drugs and their combination (O⁶BG + MX), O⁶BG was the most effective in suppressing the GBMs-on-chips.

Lastly, we sorted the drug candidates and concurrently applied CIS + KU + O⁶BG with radiation to the GBMs-on-chips. This quadruple combination was remarkably effective on the GBM-28-on-a-chip (Fig. 6e). In contrast, the GBM-37-on-a-chip constantly exhibited the high resistances to the tested drugs related to the

DNA damage response. In conclusion, we have demonstrated that the resulting ex vivo GBM model is capable of identifying the best treatment with the help of personal bioinformatics analysis.

Discussion

Our results provide proof of concept that a patient-specific ex vivo GBM model can be created through multimaterial 3D bioprinting

using the approach that we have described. By directly depositing cancer and vascular cells with BdECM bioink on a glass slide, this approach facilitated the creation of a model with a spatial tissue organization that is anatomically similar to that of a GBM. In addition, the selective use of materials with different gas-permeable properties allowed the GBM-on-a-chip to generate an oxygen gradient. This cancer model incorporated the complex ecology of GBM as well as its main pathological features. The reconstituted ecosystem reflected biochemical and biophysical cues observed in a native GBM: the heterogeneous composition of the ECM, the oxygen gradient leading to central hypoxia and the mass of cancerous tissue surrounded by dysfunctional microvessels. The potential application of this approach to produce a testing system personalized for individual patients is exemplified by the capability of reproducing patient-specific treatment resistances. Moreover, the prioritization of the tailored drug candidates shown in the GBMs-on-chips implies the possible use of this system for patient-specific drug testing.

Our approach differs substantially from conventional methods for ex vivo cultures of patient-derived cancer cells in the aspect of engineering an ecosystem that simultaneously combines biochemical and biophysical factors. Previous research on lung cancer^{7,42}, prostate cancer⁸ and circulating breast cancer cells⁴³ has demonstrated that patient-derived cancer cells have the potential to show molecular diversity and differential drug sensitivities in ex vivo culture conditions. However, because they lacked the environmental cues driving the pathological progression of the cancer, these models were less capable of reproducing the treatment response of a patient or indicating the optimal treatment approaches specific to the individual. To overcome this limitation, we used 3D-printing technology for the effective production of complex cancerous-tissue constructs⁴⁴. The 3D printing of cancers-on-chips has the potential advantages of both free-form fabrication and microfluidic manipulation^{45,46}. Owing to these abilities, our approach allows the creation of a refined model of patient-specific cancer ecology by incorporating robust heterogeneities in the cells, ECM components and the compartmentalized tissue organization associated with GBM. This is therefore a more effective tissue-level ex vivo cancer model for recreating the complex physiology of a solid tumour and for reproducing patient-specific treatment resistances when compared with conventional ex vivo cancer models. More importantly, it would be feasible to conduct point-of-care testing in a clinical setting because the 3D-printing-based approach allows the establishment of a GBM-on-a-chip within a reasonable timeframe (1–2 weeks). Given that GBM requires both an urgent and an appropriate procedure due to its extremely high lethality, the fast production of ex vivo GBM models would be a notable advantage. We expect that this approach may also be beneficial for creating models of other cancer types and eventually for guiding clinical decisions.

Methods

Preparation of the BdECM pre-gel solution. We obtained cephalic parts of market pigs that were cut along the sagittal plane from a local butcher, collected the cortex separated from the subarachnoid space and stored them at -80°C until use. For the decellularization, we cut the tissue into pieces that were $5 \times 5 \times 5$ mm in size. These small pieces were serially rinsed in sterile solutions $10\times$ the volume of the tissue. The solutions contained 100 U ml^{-1} penicillin (Sigma-Aldrich) and $100\text{ }\mu\text{g ml}^{-1}$ streptomycin (Sigma-Aldrich). The steps followed for rinsing were as follows: (1) deionized water for 48 h, (2) 0.2% sodium dodecyl sulphate (Duchefa Biochemie) in PBS (Dongin Biotech Co., Ltd.) for 24 h, (3) PBS for 15 min, (4) 50 U ml^{-1} DNase (Sigma-Aldrich) in 1 M NaCl solution for 12 h at room temperature, (5) 0.2% Triton X-100 (Biosesang) in PBS for 48–96 h, (6) PBS for 15 min and (7) 0.1% peracetic acid (Sigma-Aldrich) in 4% ethanol (Merck Millipore) for 2 h. Finally, the tissues were washed at least $8\times$ with deionized water without penicillin or streptomycin. All of these steps were conducted on a rocker at 15 r.p.m. at 4°C (except for step 4). The solutions were changed by draining the supernatant after centrifugation at 1,500 r.p.m. for 5 min. The decellularized tissue pieces were lyophilized, ground into tiny particles (<1 mm) and stored at -20°C before solubilization. The dry BdECM particles were transferred into

an HCl solution containing pepsin (1 mg mg^{-1} tissue) and digested by stirring at >300 r.p.m. for ≥ 72 h. To terminate the pepsin digestion, the acidic condition was neutralized with NaOH solution. Finally, we added $10\times$ PBS to balance the ionic strength and the ready-to-use BdECM pre-gel solution was frozen and stored for several months. For the comparative study, collagen pre-gel solution was prepared by dissolving dry collagen (medical collagen; Dalim Tissen Co., Ltd.) in HCl solution and adjusting it to the physiological conditions of pH and ionic strength.

Hydrogel-embedding culture of GBM cells and HUVECs. U-87 MG cells were cultured with high-glucose Dulbecco's Modified Eagle Medium (DMEM; GenDEPOT) containing 10% fetal bovine serum (premium, US origin; GenDEPOT) and 100 U ml^{-1} penicillin and $100\text{ }\mu\text{g ml}^{-1}$ streptomycin in a humidified 5% CO_2 incubator. HUVECs (Promocell) were cultured with Endothelial Cell Growth Medium-2 (Lonza). The culture medium was changed every 2 or 3 days. Prior to the hydrogel-embedding culture, we harvested each cell type by treating with a solution of 0.25% trypsin in EDTA (Gibco) for 3 min, collected the cells by centrifugation at 1,500 r.p.m. for 5 min and then dispersed the cells in each culture medium. The cell suspensions were mixed with the pre-gel solutions (10 mg ml^{-1}) of either BdECM or collagen to a final concentration of 5×10^6 cells ml^{-1} for both cell types. The aliquots of each cell-encapsulated pre-gel solution were transferred to the wells of a multi-well plate and placed in the incubator at 37°C for 1 h. After gelation, the culture medium for the cancer or endothelial cells was added to the wells. Each culture medium was changed every 2 or 3 days.

Cell proliferation. The level of proliferation of the cells was estimated by measuring the metabolic activities of viable cells with a Cell Counting Kit-8 assay (CCK-8; Dojindo), according to the manufacturer's instructions. Briefly, we diluted the CCK-8 agent in a fresh culture medium at a 1:10 ratio and replaced the culture medium in each well containing cell-embedded hydrogel with the agent-loaded medium. After incubation for several hours (up to 4 h), we transferred the culture medium containing the formazan dye generated by the cellular metabolism from each well to a transparent 96-well plate in quadruplicate and measured the absorbance at a wavelength of 450 nm. We conducted the CCK-8 assay at the same time on days 1, 4, 7, 10 and 14 following the culture medium changes. The values measured for each day were converted to fold changes by dividing by the value for day 1.

Invasion study using GBM-cell spheroids. GBM-28-cell spheroids were embedded in 10 mg ml^{-1} collagen or BdECM hydrogel. We prepared cell spheroids with a diameter of $\sim 200\text{ }\mu\text{m}$ using StemFIT 3D (Microfit) following the manufacturer's instructions. To implant the spheroids into the gels, we filled the wells of a 96-round-bottom microwell plate (SPL) with collagen or BdECM pre-gel solution and incubated this plate at 37°C for 10 min to partially solidify the gel beds. We then manually transferred each cancer-cell spheroid onto the top of the gel bed, covered it with the same pre-gel solution and completed the gelation. After adding the culture medium, the spheroids were maintained in the incubator. Morphological changes in the spheroids were observed after staining the F-actin with rhodamine-conjugated phalloidin and the nuclei with DAPI. The total area of fluorescence was measured with the open-source imaging processing software Image J (NIH).

Numerical analysis of oxygen concentration distribution in a GBM-on-a-chip. To estimate the spatial distribution of oxygen in a GBM-on-a-chip, we performed a finite element analysis using commercialized computational simulation software (COMSOL Multiphysics version 3.5a, COMSOL). To simulate oxygen diffusion and consumption by the cells, we applied the following governing equation, as previously described^{47,48}:

$$\frac{\partial c}{\partial t} + \nabla \cdot (-D\nabla c) = -\left(N_{\text{cell}} \frac{V_{\text{O}_2, \text{max}} c}{K_m + c}\right)$$

where c is the oxygen concentration; D denotes the diffusion coefficient of oxygen into the silicone chamber wall, culture medium or printed bioink hydrogel-containing cells; N_{cell} is the number of cells; $V_{\text{O}_2, \text{max}}$ is the maximum oxygen uptake rate of the cells, and K_m is the Michaelis–Menten constant.

We applied the following boundary conditions: (1) there was a constant supply of oxygen at a normal concentration to the cell culture incubator through the outside of the silicone chamber wall, inlet and balancing holes; (2) there was no oxygen permeation through the top and bottom of the chamber, (3) oxygen diffused through the culture medium and the solidified bioink hydrogel containing the cells and (4) the cells kept consuming the diffused oxygen. A schematic drawing of boundary conditions is presented in Supplementary Fig. 2b. The constants for each parameter are described in Supplementary Table 1.

Ink formulation and 3D-bioprinting procedures. To print a GBM-on-a-chip, we prepared a set of three kinds of inks: GBM-cell-laden bioink, HUVEC-laden bioink and silicone ink. The cell-laden bioinks were formulated by encapsulating GBM cells or HUVECs (5×10^6 cells ml^{-1}) into pre-gel solutions of BdECM or collagen (10 mg ml^{-1}). The cell-laden bioinks were then loaded into 1-ml disposable syringes

and were pre-chilled at 4 °C before starting the printing process. The silicone ink was prepared using a modification of a previously reported method⁴⁵. We blended the elastomer base (Shin-Etsu Silicone) with the curing agent at a 10:1 volume ratio and loaded the mixture into a 10-ml clear syringe (PSY-E; Musashi Engineering, Ltd.). Our in-house 3D-printing system⁴⁹ has multiple slots for printing heads; we therefore loaded the three types of prepared inks into different slots for the sequential printing process following the specified steps. The head for the silicone ink was connected to an air pressure controller (Super Sigma X-V7; Musashi Engineering, Ltd.) and the ink was extruded at a pressure of 200–400 kPa for the 20 G taper nozzle (Musashi Engineering, Ltd.). The heads for the cell-laden bioinks were connected to the plungers of the bioink-loaded syringes; these were pushed down at a speed of approximately 500 nls⁻¹ for the 26 G flat needle (Musashi Engineering, Ltd.) attached to the syringe. The speed of the pushing motion was regulated by a linear motor controller (Nano Master SMP-III; Musashi Engineering, Ltd.). The printing system was operated by a numerical control program (Supplementary Source Code). This program specified the paths and moving speeds of the printing heads in the *x*, *y* and *z* directions, as well as the on/off switching sequence of the controllers. The printing inks were deposited on a sterilized surface-modified slide glass (Matsunami Adhesive Slide, Matsunami Ind., Ltd.). The printing procedures were all conducted in a cool atmosphere at 18 °C. To prevent the cell-printed construct from drying out, we covered the chamber with a glass cover slip immediately after printing. The printed chip was incubated in a humidified condition (37 °C) for 1 h. The culture medium was changed every day.

Analysis of mRNA expression analysis by real-time PCR. After a single PBS wash of the GBMs-on-chips, we replaced all of the media in the chamber with RNAiso Plus (Takara). We then collected the lysate and isolated the total RNA from each chip, following the manufacturer's protocol. After measuring the RNA concentrations using a Nanodrop (Thermo Scientific), we synthesized the complementary DNAs with a Maxima First Strand cDNA Synthesis kit for RT-qPCR (Thermo Fisher Scientific), following the manufacturer's instructions. To commence the real-time PCR, we used a SYBR Green PCR Master Mix assay (Applied Biosystems) with primers to the complementary DNA samples and ran three-step cycles for the amplification reaction using a Light Cycler 480 (Roche). The fold changes of the target genes were calculated according to the 2^{-ΔΔC_t} method by normalizing to the expression of a housekeeping gene, *GAPDH*. The primer sequences were designed following the National Center for Biotechnology Information reference sequences for each nucleotide: NM_001256799.2 for *GAPDH*, NM_001025366.2 for *VEGFA*, NM_001168298.1 for *IL8*, NM_001199649.1 for *PTK2*, NM_001306129.1 for *FN*, NM_001145938.1 for *MMP1*, NM_001127891.2 for *MMP2*, NM_004994.2 for *MMP9*, NM_000442.4 for *PECAM1*, NM_001795.4 for *CDH5*, NM_001301025.1 for *TJPI*, NM_001243084.1 for *HIF1A*, NM_001145966.1 for *MKI67*, NM_001166356.1 for *SHMT2*, NM_001168298.1 for *CXCR2*, NM_003106.3 for *SOX2*, NM_001145848.1 for *PROM1* and NM_006617.1 for *NES*.

Histology and DAPI staining. To evaluate the efficiency of the decellularization, we performed haematoxylin and eosin staining and DAPI staining (1:1,000 dilution in PBS) of frozen sections of the native brain tissue and BdeCM that were approximately 10-μm thick.

Immunostaining. To detect the specified molecules in the cells, we performed immunostaining of the samples obtained from the hydrogel-embedding culture and the GBMs-on-chips, following a modification of a previously reported procedure²². All of the samples were fixed with 4% paraformaldehyde for 20 min, permeabilized with 0.1% Triton X-100 in PBS for 5 min and blocked with 20% goat serum for 1 h at room temperature. The primary antibodies diluted in PBS were added to the samples and incubated overnight at 4 °C. The samples were washed with PBS and placed on a rocker at 10 r.p.m., which was filled with PBS and maintained at 4 °C overnight. The secondary antibodies and/or DAPI were diluted in PBS and incubated with the samples for 6 h at 4 °C. The dilution ratios are given in Supplementary Table 2. The samples were again washed with PBS overnight on the shaker at 4 °C. Finally, we observed the samples using a confocal microscope (TCS SP8 X, Leica).

The cells that experienced hypoxia were detected using a Hypoxyprobe-1 Plus kit (Hypoxyprobe, Inc.), following the manufacturer's instructions with a modification we previously described¹⁷. We added pimonidazole into the culture medium 24 h before harvesting the samples. Cells under hypoxic conditions (14 μM) form adducts with pimonidazole; we therefore detected these adducts on the basis of the binding with FITC-conjugated antibody after fixation, permeabilization and blocking with the same reagent used for the other immunostaining procedures. We observed the samples using a fluorescent microscope.

Ethics statements. We obtained informed consent from the patients for taking fresh GBM samples and accessing their clinical records. This study was approved by the Institutional Review Board of the Seoul National University Hospital (IRB no. H-0507-509-153).

Primary GBM culture. GBM samples were obtained during tumour excision surgery and were dissociated into single cells using papain digestion, as previously

described⁵⁰. Briefly, the primary cells were cultured with DMEM containing 10% fetal bovine serum and 100 U ml⁻¹ penicillin and 100 μg ml⁻¹ streptomycin in the cell culture incubator. The culture medium was changed every 2 or 3 days.

Bioinformatics analysis. Total RNA was isolated from GBM-28 and -37 cells (<10 passages) and the transcriptomic profiles were identified by an oligonucleotide microarray analysis with MA-human Agilent 44 K (Agilent Technologies). We applied a global median normalization method to analyse the one-channel microarray data using GeneSpring GX 7.3 (EBIOGEN). We then uploaded the cDNA microarray data into the GSEA (Desktop Application, version 2.1.0; Broad Institute, Inc.) to determine the differentially enriched gene sets in the GBM-28 and -37 cells. The GSEA was performed using the pre-ranked tool based on the genes that were ranked differentially between the GBM-28 and -37 cells and Reactome gene sets (version 5.2). The data were permuted 1,000 times and the subsequent enrichment score, normalized enrichment score, nominal *P* value and false discovery rate (*q* value) were obtained to identify the gene sets that were significantly enriched in either phenotype. The leading edge subset from the GSEA was further analysed using the core analysis option of the Ingenuity Pathway Analysis (IPA) software package (version 8.7; QIAGEN). The Ingenuity Knowledge Base contains the largest database of manually curated and experimentally validated interactions among genes and proteins based on their physical, transcriptional and molecular interactions. An enrichment *P* value (obtained using the Fisher's exact test) was calculated within IPA to identify pathways associated with the given gene set.

The measurement of surviving fractions of the GBMs-on-chips. To simulate CCRT with anti-cancer drugs, we applied culture media containing the drugs to the patient-specific GBMs-on-chips that had been cultured for seven days and transferred them to a gamma irradiator (Gammacell 3000 Elan, MDS Nordion) within 1 h. After the irradiation, the chips were placed back in the cell culture incubator for 24 h. The drug-loaded culture media were then substituted with fresh media containing the CCK-8 assay agent at a volume ratio of 10:1. After a reaction time of 2–4 h, we collected the medium from each patient-specific GBM-on-a-chip, measured the absorbance at a wavelength of 450 nm and estimated the surviving fractions by comparing the values measured in the treatment groups with those from no treatment groups.

Statistical analysis. All data are presented as the mean ± s.d. For the statistical analysis of all experimental results, except for those involving GSEA and IPA, we performed paired two-tailed Student's *t*-tests to compare two groups. For comparisons of three or more groups, we performed one-way ANOVAs with subsequent Bonferroni post-hoc testing when the *F* value rejected the null hypothesis. We considered differences to be statistically significant when *P* < 0.05.

Reporting Summary. Further information on research design is available in the Reporting Summary linked to this article.

Code availability

The computer code for the bioprinting of the GBM-on-a-chip is provided as Supplementary Information.

Data availability

The authors declare that all data supporting the results in this study are available within the paper and its Supplementary information. The source data for the figures in this study are available from figshare (identifier <https://doi.org/10.6084/m9.figshare.7392677>)⁵¹.

Received: 26 July 2017; Accepted: 5 February 2019;

Published online: 18 March 2019

References

- Schreiber, S. L. et al. Towards patient-based cancer therapeutics. *Nat. Biotechnol.* **28**, 904–906 (2010).
- Al-Lazikani, B., Banerji, U. & Workman, P. Combinatorial drug therapy for cancer in the post-genomic era. *Nat. Biotechnol.* **30**, 679–692 (2012).
- Creixell, P., Schoof, E. M., Erler, J. T. & Lindner, R. Navigating cancer network attractors for tumor-specific therapy. *Nat. Biotechnol.* **30**, 842–848 (2012).
- Aparicio, S., Hidalgo, M. & Kung, A. L. Examining the utility of patient-derived xenograft mouse models. *Nat. Rev. Cancer* **15**, 311–316 (2015).
- Eirew, P. et al. Dynamics of genomic clones in breast cancer patient xenografts at single-cell resolution. *Nature* **518**, 422–426 (2015).
- Byrne, A. T. et al. Interrogating open issues in cancer precision medicine with patient-derived xenografts. *Nat. Rev. Cancer* **17**, 254–268 (2017).
- Crystal, A. S. et al. Patient-derived models of acquired resistance can identify effective drug combinations for cancer. *Science* **346**, 1480–1486 (2014).
- Gao, D. et al. Organoid cultures derived from patients with advanced prostate cancer. *Cell* **159**, 176–187 (2014).

9. Hanahan, D. & Coussens, L. M. Accessories to the crime: functions of cells recruited to the tumor microenvironment. *Cancer Cell* **21**, 309–322 (2012).
10. Sackmann, E. K., Fulton, A. L. & Beebe, D. J. The present and future role of microfluidics in biomedical research. *Nature* **507**, 181–189 (2014).
11. Picollet-D'hahan, N. et al. A 3D toolbox to enhance physiological relevance of human tissue models. *Trends Biotechnol.* **34**, 757–769 (2016).
12. Garber, K. Between disease and a dish. *Nat. Biotechnol.* **32**, 712–715 (2014).
13. Yamada, K. M. & Cukierman, E. Modeling tissue morphogenesis and cancer in 3D. *Cell* **130**, 601–610 (2007).
14. Lathia, J. D., Heddleston, J. M., Venero, M. & Rich, J. N. Deadly teamwork: neural cancer stem cells and the tumor microenvironment. *Cell Stem Cell* **8**, 482–485 (2011).
15. Junttila, M. R. & de Sauvage, F. J. Influence of tumour micro-environment heterogeneity on therapeutic response. *Nature* **501**, 346–354 (2013).
16. Korolev, K. S., Xavier, J. B. & Gore, J. Turning ecology and evolution against cancer. *Nat. Rev. Cancer* **14**, 371–380 (2014).
17. Ananthanarayanan, B., Kim, Y. & Kumar, S. Elucidating the mechanobiology of malignant brain tumors using a brain matrix-mimetic hyaluronic acid hydrogel platform. *Biomaterials* **32**, 7913–7923 (2011).
18. Kievit, F. M. et al. Chitosan–alginate 3D scaffolds as a mimic of the glioma tumor microenvironment. *Biomaterials* **31**, 5903–5910 (2010).
19. Lee, G. Y., Kenny, P. A., Lee, E. H. & Bissell, M. J. Three-dimensional culture models of normal and malignant breast epithelial cells. *Nat. Methods* **4**, 359–365 (2007).
20. Pedron, S., Becka, E. & Harley, B. A. Spatially graded hydrogel platform as a 3D engineered tumor microenvironment. *Adv. Mater.* **27**, 1567–1572 (2015).
21. Bhatia, S. N. & Ingber, D. E. Microfluidic organs-on-chips. *Nat. Biotechnol.* **32**, 760–772 (2014).
22. Shin, Y. et al. Microfluidic assay for simultaneous culture of multiple cell types on surfaces or within hydrogels. *Nat. Protoc.* **7**, 1247–1259 (2012).
23. Ostrom, Q. T. et al. CBTRUS statistical report: primary brain and other central nervous system tumors diagnosed in the United States in 2009–2013. *Neuro Oncol.* **18**, v1–v75 (2016).
24. Ott, H. C. et al. Perfusion-decellularized matrix: using nature's platform to engineer a bioartificial heart. *Nat. Med.* **14**, 213–221 (2008).
25. Chen, H. J. et al. A recellularized human colon model identifies cancer driver genes. *Nat. Biotechnol.* **34**, 845–851 (2016).
26. Dunne, L. W. et al. Human decellularized adipose tissue scaffold as a model for breast cancer cell growth and drug treatments. *Biomaterials* **35**, 4940–4949 (2014).
27. Pati, F. et al. Printing three-dimensional tissue analogues with decellularized extracellular matrix bioink. *Nat. Commun.* **5**, 3935 (2014).
28. Choi, Y.-J. et al. 3D cell printing of functional skeletal muscle constructs using skeletal muscle-derived bioink. *Adv. Healthc. Mater.* **5**, 2636–2645 (2016).
29. Le, P. U. et al. DRR drives brain cancer invasion by regulating cytoskeletal-focal adhesion dynamics. *Oncogene* **29**, 4636–4647 (2010).
30. Jung, J. W., Lee, J.-S. & Cho, D.-W. Computer-aided multiple-head 3D printing system for printing of heterogeneous organ/tissue constructs. *Sci. Rep.* **6**, 21685 (2016).
31. Kim, D. et al. SHMT2 drives glioma cell survival in ischaemia but imposes a dependence on glycine clearance. *Nature* **520**, 363–367 (2015).
32. Jain, R. K. et al. Angiogenesis in brain tumours. *Nat. Rev. Neurosci.* **8**, 610–622 (2007).
33. Brandes, A. A. et al. First-line chemotherapy with cisplatin plus fractionated temozolomide in recurrent glioblastoma multiforme: a phase II study of the Gruppo Italiano Cooperativo di Neuro-oncologia. *J. Clin. Oncol.* **22**, 1598–1604 (2004).
34. Bao, Q. et al. Recombinant TIMP-1-GPI inhibits growth of fibrosarcoma and enhances tumor sensitivity to doxorubicin. *Target. Oncol.* **9**, 251–261 (2014).
35. McFaline-Figueroa, J. L. et al. Minor changes in expression of the mismatch repair protein MSH2 exert a major impact on glioblastoma response to temozolomide. *Cancer Res.* **75**, 3127–3138 (2015).
36. Munoz, J. L. et al. Temozolomide resistance in glioblastoma cells occurs partly through epidermal growth factor receptor-mediated induction of connexin 43. *Cell Death Dis.* **5**, e1145 (2014).
37. Perazzoli, G. et al. Temozolomide resistance in glioblastoma cell lines: implication of MGMT, MMR, P-glycoprotein and CD133 expression. *PLoS ONE* **10**, e0140131 (2015).
38. Hirose, Y., Berger, M. S. & Pieper, R. O. Abrogation of the Chk1-mediated G2 checkpoint pathway potentiates temozolomide-induced toxicity in a p53-independent manner in human glioblastoma cells. *Cancer Res.* **61**, 5843–5849 (2001).
39. Vecchio, D. et al. Predictability, efficacy and safety of radiosensitization of glioblastoma-initiating cells by the ATM inhibitor KU-60019. *Int. J. Cancer* **135**, 479–491 (2014).
40. Hegi, M. E. et al. Clinical trial substantiates the predictive value of O-6-methylguanine-DNA methyltransferase promoter methylation in glioblastoma patients treated with temozolomide. *Clin. Cancer Res.* **10**, 1871–1874 (2004).
41. Eads, J. R. et al. Phase I clinical trial of temozolomide and methoxyamine (TRC-102) in patients with advanced solid tumors. *J. Clin. Oncol.* **33**, 2558–2558 (2015).
42. Xu, Z. et al. Application of a microfluidic chip-based 3D co-culture to test drug sensitivity for individualized treatment of lung cancer. *Biomaterials* **34**, 4109–4117 (2013).
43. Yu, M. et al. Ex vivo culture of circulating breast tumor cells for individualized testing of drug susceptibility. *Science* **345**, 216–220 (2014).
44. Choi, Y.-J., Yi, H.-G., Kim, S.-W. & Cho, D.-W. 3D cell printed tissue analogues: a new platform for theranostics. *Theranostics* **7**, 3118–3137 (2017).
45. Lind, J. U. et al. Instrumented cardiac microphysiological devices via multimaterial three-dimensional printing. *Nat. Mater.* **16**, 303–308 (2016).
46. Lee, H. & Cho, D.-W. One-step fabrication of an organ-on-a-chip with spatial heterogeneity using a 3D bioprinting technology. *Lab Chip* **16**, 2618–2625 (2016).
47. Kang, T.-Y., Hong, J. M., Jung, J. W., Yoo, J. J. & Cho, D.-W. Design and assessment of a microfluidic network system for oxygen transport in engineered tissue. *Langmuir* **29**, 701–709 (2013).
48. Jung, J. W. et al. Evaluation of the effective diffusivity of a freeform fabricated scaffold using computational simulation. *J. Biomech. Eng.* **135**, 084501 (2013).
49. Kim, J. Y. & Cho, D.-W. Blended PCL/PLGA scaffold fabrication using multi-head deposition system. *Microelectron. Eng.* **86**, 1447–1450 (2009).
50. Jo, H. Y. et al. The unreliability of MTT assay in the cytotoxic test of primary cultured glioblastoma cells. *Exp. Neurobiol.* **24**, 235–245 (2015).
51. Yi, H.-G. et al. A bioprinted human-glioblastoma-on-a-chip reproduces patient-specific responses to chemoradiotherapy. *Figshare* <https://doi.org/10.6084/m9.figshare.7392677> (2018).

Acknowledgements

This work was supported by the National Research Foundation of Korea (NRF) funded by the Korean government, MSIP (grant nos 2010-0018294, 2015R1A2A2A01005515 and 2018R1A2B2009540). This study was partly supported by the Technology Innovation Program (grant no. 10050154, Business Model Development for Personalized Medicine Based on Integrated Genome and Clinical Information) and by the Bio and Medical Technology Development Program of the NRF funded by the Korean government, MSIP (grant no. 2015M3C7A1028926). We thank J. M. Hong for technical assistance and M. N. Park for helpful discussions.

Author contributions

H.-G.Y., D.-W.C. and S.H.Paek conceived the concept of applying 3D-printing technology to establish the patient-specific GBM-on-a-chip. H.-G.Y. and Y.H.J. devised the working principles of the chip in detail. H.-G.Y. designed and performed most of the experiments. Y.K. performed the bioinformatics analyses and wrote the relevant results and methods. Y.-J.C. assisted with the characterization of the BdECM bioink, 3D printing of the GBMs-on-chips and performed the tumour spheroid invasion study. H.E.M. prepared for the IRB approval process to conduct the experiments using patient-derived GBM cells and organized the clinical information of the patients. S.H.Paek was the physician in charge of the GBM patients. S.H.Paek performed the pathological detection and analysis of the patient-derived GBMs. K.S.K. contributed to the discussion for the initial stages of this work. M.B. assisted with the 3D printing and culturing of the GBMs-on-chips. J.J. contributed to the discussion for the revisions of the manuscript. H.Y. provided the genetic analysis data of patient-derived GBM cells. H.-G.Y., Y.H.J., S.H.Paek and D.-W.C. analysed the data. S.H.Paek also analysed the clinical observations and provided the relevant consultation. D.-W.C. provided overall guidance and supervised the project. H.-G.Y. and Y.H.J. wrote and edited the manuscript.

Competing interests

Patents on the use of BdECM bioink in modelling cancer (patent no. 10-1860798, Korea) and on 3D printing of GBM-on-a-chip (patent no. 10-1803618, Korea) have been registered.

Additional information

Supplementary information is available for this paper at <https://doi.org/10.1038/s41551-019-0363-x>.

Reprints and permissions information is available at www.nature.com/reprints.

Correspondence and requests for materials should be addressed to S.H.P. or D.-W.C.

Publisher's note: Springer Nature remains neutral with regard to jurisdictional claims in published maps and institutional affiliations.

© The Author(s), under exclusive licence to Springer Nature Limited 2019

Reporting Summary

Nature Research wishes to improve the reproducibility of the work that we publish. This form provides structure for consistency and transparency in reporting. For further information on Nature Research policies, see [Authors & Referees](#) and the [Editorial Policy Checklist](#).

Statistics

For all statistical analyses, confirm that the following items are present in the figure legend, table legend, main text, or Methods section.

- | n/a | Confirmed |
|-------------------------------------|--|
| <input type="checkbox"/> | <input checked="" type="checkbox"/> The exact sample size (n) for each experimental group/condition, given as a discrete number and unit of measurement |
| <input type="checkbox"/> | <input checked="" type="checkbox"/> A statement on whether measurements were taken from distinct samples or whether the same sample was measured repeatedly |
| <input type="checkbox"/> | <input checked="" type="checkbox"/> The statistical test(s) used AND whether they are one- or two-sided
<i>Only common tests should be described solely by name; describe more complex techniques in the Methods section.</i> |
| <input type="checkbox"/> | <input checked="" type="checkbox"/> A description of all covariates tested |
| <input checked="" type="checkbox"/> | <input type="checkbox"/> A description of any assumptions or corrections, such as tests of normality and adjustment for multiple comparisons |
| <input type="checkbox"/> | <input checked="" type="checkbox"/> A full description of the statistical parameters including central tendency (e.g. means) or other basic estimates (e.g. regression coefficient) AND variation (e.g. standard deviation) or associated estimates of uncertainty (e.g. confidence intervals) |
| <input type="checkbox"/> | <input checked="" type="checkbox"/> For null hypothesis testing, the test statistic (e.g. F , t , r) with confidence intervals, effect sizes, degrees of freedom and P value noted
<i>Give P values as exact values whenever suitable.</i> |
| <input checked="" type="checkbox"/> | <input type="checkbox"/> For Bayesian analysis, information on the choice of priors and Markov chain Monte Carlo settings |
| <input checked="" type="checkbox"/> | <input type="checkbox"/> For hierarchical and complex designs, identification of the appropriate level for tests and full reporting of outcomes |
| <input checked="" type="checkbox"/> | <input type="checkbox"/> Estimates of effect sizes (e.g. Cohen's d , Pearson's r), indicating how they were calculated |

Our web collection on [statistics for biologists](#) contains articles on many of the points above.

Software and code

Policy information about [availability of computer code](#)

Data collection

N/A

Data analysis

Microsoft Excel was used to analyse the data.

For manuscripts utilizing custom algorithms or software that are central to the research but not yet described in published literature, software must be made available to editors/reviewers. We strongly encourage code deposition in a community repository (e.g. GitHub). See the Nature Research [guidelines for submitting code & software](#) for further information.

Data

Policy information about [availability of data](#)

All manuscripts must include a [data availability statement](#). This statement should provide the following information, where applicable:

- Accession codes, unique identifiers, or web links for publicly available datasets
- A list of figures that have associated raw data
- A description of any restrictions on data availability

The authors declare that all data supporting the results in this study are available within the paper and its Supplementary Information. Source data for the figures in this study are available from figshare with the identifier <https://doi.org/10.6084/m9.figshare.7392677> (ref. 51).

Field-specific reporting

Please select the one below that is the best fit for your research. If you are not sure, read the appropriate sections before making your selection.

- Life sciences Behavioural & social sciences Ecological, evolutionary & environmental sciences

Life sciences study design

All studies must disclose on these points even when the disclosure is negative.

Sample size	No statistical analyses were performed to predetermine sample sizes, but the sample sizes used are similar to those generally employed in the field.
Data exclusions	No data were excluded from the analyses.
Replication	All attempts at replication were successful for each series of the experiments.
Randomization	Randomization of experimental groups was not required for this study.
Blinding	Blinding was not applicable to this study.

Reporting for specific materials, systems and methods

We require information from authors about some types of materials, experimental systems and methods used in many studies. Here, indicate whether each material, system or method listed is relevant to your study. If you are not sure if a list item applies to your research, read the appropriate section before selecting a response.

Materials & experimental systems

n/a	Involved in the study
<input type="checkbox"/>	<input checked="" type="checkbox"/> Antibodies
<input type="checkbox"/>	<input checked="" type="checkbox"/> Eukaryotic cell lines
<input checked="" type="checkbox"/>	<input type="checkbox"/> Palaeontology
<input type="checkbox"/>	<input checked="" type="checkbox"/> Animals and other organisms
<input type="checkbox"/>	<input checked="" type="checkbox"/> Human research participants
<input checked="" type="checkbox"/>	<input type="checkbox"/> Clinical data

Methods

n/a	Involved in the study
<input checked="" type="checkbox"/>	<input type="checkbox"/> ChIP-seq
<input checked="" type="checkbox"/>	<input type="checkbox"/> Flow cytometry
<input checked="" type="checkbox"/>	<input type="checkbox"/> MRI-based neuroimaging

Antibodies

Antibodies used

We used the following primary antibodies: rabbit polyclonal antibody to human CD31 (Abcam; catalog number ab28364), rabbit polyclonal antibody to human Ki67 (Abcam; catalog number ab15580; lot number GR2576688-2), mouse polyclonal antibody to human SHMT2 (Abcam; catalog number ab88664; lot number GR101362-3), and mouse monoclonal antibody to human SOX2 (Abcam; catalog number ab75485). These are described in the Supplementary information section of the paper. Statements related to the specificity and the species reactivity of each antibody are provided through the manufacturer's website (<http://www.abcam.com>).

We used the following secondary antibodies: goat anti-rabbit IgG secondary antibody (Alexa Fluor 488; Molecular Probes; catalog number A11008; lot number 1853312), goat anti-rabbit IgG secondary antibody (Alexa Fluor 594; Molecular Probes; catalog number A11012; lot number 1844440A), goat anti-mouse IgG secondary antibody (Alexa 488; Molecular Probes; catalog number A11001; lot number 1834337), and goat anti-mouse IgG secondary antibody (Alexa 594; Molecular Probes; catalog number A11005; lot number 1796406).

Validation

The manufacturer provided validation data for each lot number.

Eukaryotic cell lines

Policy information about [cell lines](#)

Cell line source(s)

We used the U-87 MG cell line (American Type Culture Collection (ATCC); catalog number HTB-14; lot number 58492108).

Authentication

According to ATCC's certificate of analysis for this lot (No. 58492108), short tandem repeat (STR) DNA analysis was performed, and the resulting profile corresponded to that of ATCC's original stock.

Mycoplasma contamination

According to ATCC's certificate of analysis for this lot (No. 58492108), Hoechst DNA stain and agar culture did not detect mycoplasma contamination.

Commonly misidentified lines
(See [ICLAC](#) register)

Although ATCC authenticated that the provided stock corresponded to their original stock, the STR profiling identified that the ATCC version of U-87 MG cell line is different from that of Uppsala University's collection. Therefore, Allen et al. (Science Translational Medicine; 8:354; 354re3) articulated that ATCC's U-87 MG cell line is likely to be a bona fide human glioblastoma cell line of unknown origin.

Animals and other organisms

Policy information about [studies involving animals](#); [ARRIVE guidelines](#) recommended for reporting animal research

Laboratory animals	The study did not involve laboratory animals.
Wild animals	To produce the porcine brain decellularized extracellular matrix, we purchased the cephalic parts of market pig from the local butcher's shop (Suji Food, Business registration No. 219-19-65592, Incheon, Korea).
Field-collected samples	The female pigs (age of 5–6 months) reaching a final weight (~280 lbs) in a pig farm were sent to a packing plant to be harvested following a guideline of the Ministry of Agriculture, Food and Rural Affairs of Korea.
Ethics oversight	No ethical approval was required because we used market pig produced following a guideline of the Ministry of Agriculture, Food and Rural Affairs of Korea.

Note that full information on the approval of the study protocol must also be provided in the manuscript.

Human research participants

Policy information about [studies involving human research participants](#)

Population characteristics	<p>Patient (a) was a 42-year-old female with glioblastoma. She received craniotomy and chemoradiation therapy with temozolomide. She survived 110.7 weeks following the initial diagnosis of glioblastoma and exhibited a low treatment resistance to the treatment.</p> <p>Patient (b) was a 33-year-old male with glioblastoma. He received craniotomy and chemoradiation therapy with temozolomide. He survived more than six years following the initial diagnosis of glioblastoma and exhibited a favorable outcome after receiving the treatment.</p> <p>Patient (c) was a 41-year-old male with glioblastoma. He received craniotomy and chemoradiation therapy with temozolomide. He survived 140 weeks following the initial diagnosis of glioblastoma and exhibited a low treatment resistance to the treatment.</p> <p>Patient (d) was a 76-year-old female with a diagnosis of glioblastoma in 2013. She received craniotomy and chemoradiation therapy with temozolomide. She was less sensitive to the treatment and survived 34.3 weeks after the initial diagnosis. As the WHO classification of tumors of the central nervous system newly added molecular parameters for a diagnosis, oligodendroglioma would be appropriate for the current diagnosis of the patient.</p> <p>Patient (e) was a 59-year-old female with glioblastoma. She received craniotomy and chemoradiation therapy with temozolomide. The patient was less sensitive to the treatment and survived less than 52 weeks following the initial diagnosis of glioblastoma.</p> <p>Patient (f) was a 44-year-old female with glioblastoma. She received craniotomy and chemoradiation therapy with temozolomide. She survived 45.1 weeks after the initial diagnosis showed very aggressive progression following the treatment.</p> <p>Patient (g) was a 71-year-old female with glioblastoma. She received craniotomy and chemoradiation therapy with temozolomide. She survived 71 weeks after the initial diagnosis showed very aggressive progression following the treatment.</p>
Recruitment	We recruited patients who agreed to provide their GBM specimen during tumour-removal surgery. We obtained informed consent from the patients for taking the fresh human GBM samples.
Ethics oversight	The study was approved by the Institutional Review Board of Seoul National University Hospital (IRB number: H-0507-509-153).

Note that full information on the approval of the study protocol must also be provided in the manuscript.